Research Square

Preprints are preliminary reports that have not undergone peer review.
They should not be considered conclusive, used to inform clinical practice,
or referenced by the media as validated information.

Dual-Function Molecularly Imprinted Polypyrrole Enables Adhesion-Layer- Free Gold Nanostructures for Selective, Antifouling Dopamine Monitoring during Neuronal Differentiation

Joon-Ha Park
Sungkyunkwan University (SKKU)
Yeon-Woo Cho
Sungkyunkwan University (SKKU)
Min-ji Kang
Sungkyunkwan University (SKKU)
Eun-Cheol Kwak
Sungkyunkwan University (SKKU)
Tae-Hyung Kim
thkim0512@skku.edu

Sungkyunkwan University (SKKU)

Research Article

Keywords: Molecularly imprinted polymer, Gold nanostructure, Dopamine sensing, Polypyrrole, Dopaminergic differentiation

Posted Date: September 9th, 2026

DOI: https://doi.org/10.21203/rs.3.rs-10828818/v1

License: This work is licensed under a Creative Commons Attribution 4.0 International License.
Read Full License

Additional Declarations: No competing interests reported.

Abstract

Direct electrochemical detection of extracellular dopamine (DA) in complex biological media remains challenging because of biofouling and the limited mechanical durability of nanostructured sensing interfaces. Here, an all-electrochemical strategy that integrates electrodeposited gold nanostructures (AuNSs) with a DA-imprinted polypyrrole (PPy) layer is presented. Uniquely, the conformal PPy coating serves a dual function by simultaneously providing molecular recognition and mechanically anchoring the underlying AuNSs, thereby eliminating the need for conventional adhesion layers while preserving structural integrity during repeated operation. The resulting sensor exhibits linear responses over 0.01–20 μM (limit of detection: 57.4 nM) in phosphate-buffered saline (PBS) and 0.05– 20 μM (83.6 nM) in 10% serum-supplemented culture medium. Owing to its antifouling imprinted interface, the sensor retains 71.8% of its initial signal after operation in serum-supplemented medium, whereas bare AuNS electrodes retain only 5.6%, while also exhibiting excellent selectivity against coexisting interferents. The platform enables direct quantification of stimulus-evoked DA release from untreated culture supernatants, allowing dynamic profiling throughout SH-SY5Y neuronal differentiation, in excellent agreement with both HPLC and ELISA. Beyond DA sensing, this work establishes a generalizable strategy for integrating molecularly imprinted polymers with nanostructured electrodes to create mechanically robust, selective, and antifouling biointerfaces for long-term cell-based electrochemical sensing.

1 Introduction

Functional maturation of dopaminergic (DAergic) neurons is ultimately defined by their ability to synthesize and release dopamine (DA) [1-3]. Because lineage-specific markers can be expressed before cells acquire the capacity for stimulus-evoked DA secretion, marker profiling alone cannot establish functional maturation [4-8]. Direct quantification of extracellular DA therefore provides an important functional readout of the DAergic phenotype [9-13]. Despite its biological significance, quantitative analysis of extracellular DA remains technically challenging because it requires rapid, selective detection directly in complex culture media with minimal sample processing [14-19].

Conventional analytical methods do not fully satisfy these requirements. High-performance liquid chromatography (HPLC) offers excellent analytical accuracy but requires sample handling and chromatographic separation, during which DA readily undergoes autoxidation, leading to underestimation of its original extracellular concentration [20-21]. Enzyme-linked immunosorbent assays (ELISAs) are highly sensitive but rely on lengthy incubation steps, while the high-potassium buffers used to stimulate DA secretion perturb antibody-analyte interactions and introduce matrix-dependent bias [22-25]. Electrochemical detection enables rapid and direct analysis with minimal sample preparation; however, the direct oxidation of DA in biological media is compromised by structurally related electroactive interferents and severe electrode passivation caused by adsorbed proteins and oxidation by-products [26-35]. Consequently, electrochemical measurement of DA in cell-culture supernatants

requires a sensing interface that combines molecular selectivity, high sensitivity, and robust resistance to biofouling.

Signal amplification using carbon nanomaterials, metallic nanostructures, or conductive polymers can improve electrochemical sensitivity, but it cannot by itself discriminate DA from structurally related catecholamines such as epinephrine and norepinephrine [36-40]. Biological recognition elements, including antibodies and aptamers, provide molecular specificity but require complex synthesis and immobilization, and their binding behaviour can be affected by ionic strength and media composition [41-44]. Molecularly imprinted polymers (MIPs) provide a compelling synthetic alternative [45-49]. Polymerization around a molecular template followed by template extraction generates artificial recognition cavities complementary in size, shape, and chemical functionality to the target, enabling label-free molecular recognition with greater chemical and environmental stability than biological receptors.

In addition to molecular recognition, a practical electrochemical sensor must maintain structural integrity during fabrication and repeated operation [50-54]. This requirement is particularly challenging for electrodeposited metallic nanostructures, which provide high electrochemical activity but often adhere weakly to oxide substrates and may delaminate during the repeated potential cycling required for electropolymerization, template extraction, and sensing. Conventional approaches typically rely on sputtered Cr or Ti adhesion layers, adding vacuum-processing steps and potentially altering interfacial electrochemical properties [55-56]. An entirely electrochemical strategy that simultaneously provides molecular recognition and mechanically stabilizes the nanostructured transducer would therefore offer a substantial advantage.

This work presents an adhesion-layer-free electrochemical platform in which a DA-imprinted polypyrrole (PPy) coating serves a dual function as both a molecular-recognition interface and a mechanical anchor for an electrodeposited gold nanostructure (AuNS). The platform is fabricated by sequential electrodeposition of a high-surface-area AuNS onto indium tin oxide (ITO), followed by conformal in situ electropolymerization of the DA-imprinted PPy layer **(Fig. 1)**. This all-electrochemical architecture integrates efficient signal transduction, molecular selectivity, mechanical durability, and resistance to protein fouling within a single sensing interface. The optimized sensor enables direct quantification of DA in serum-containing culture medium while retaining more than 70% of its response under conditions in which bare AuNS electrodes retain only 5.6%. Its practical utility was demonstrated by monitoring stimulus-evoked extracellular DA release from SH-SY5Y cells throughout a 12-day differentiation period using untreated culture supernatants, with the measured concentrations independently validated by HPLC and ELISA. These findings establish a practical approach for quantitative assessment of functional DAergic maturation and provide a general strategy for integrating molecularly imprinted recognition layers with mechanically robust nanostructured electrochemical interfaces.

2 Results and Discussion

2.1 Fabrication, structural characterization, and anchoring of the DA-imprinted MIP electrode

Trace-level DA detection requires an electrochemical interface that combines efficient charge transfer with resistance to biofouling. Because ITO modified with NIP or MIP lacked sufficient sensitivity to detect physiological levels of DA in both PBS and complex medium **(Fig. S1a-f)**, the sensing interface was fabricated through a simple two-step, entirely electrochemical process. First, a conductive AuNS was electrodeposited onto ITO to enhance interfacial electron-transfer kinetics. This was followed by in situ electropolymerization of a DA-imprinted PPy layer, which provides both molecular selectivity and resistance to protein fouling **(Fig. 2a)**. Notably, the entire architecture was constructed without a sputtered adhesion layer or any vacuum-deposition step. As described below, the conformal PPy overlayer serves as a mechanical anchor for the underlying AuNS, preserving the nanostructured interface throughout electrochemical fabrication and enabling rapid, all-electrochemical assembly. Unless stated otherwise, all electrodes were prepared under the conditions optimized in Section 2.2: 0.5 mM DA, 5 mM Py, 10 electropolymerization cycles, and template extraction with MeOH/acetic acid (6:4, v/v).

The stepwise assembly was tracked with a 5 mM $[Fe(CN)6]^{3-/4-}$ redox probe **(Fig. 2b,c)**. Gold deposition raised the peak currents by 34% (A→B; **Fig. S2a, b**), which, according to the Randles–Ševčík equation ($i_p \propto n^{3/2}AD^{1/2}Cv^{1/2}$), reflects the enlarged electrochemically active surface area (ECSA) of the nanostructured gold. Subsequent growth of the imprinted-polymer (C) reduced the current by 99%, consistent with near-complete encapsulation of the gold surface by the poorly conductive overoxidized PPy matrix. Following template extraction (D), the current recovered to approximately 60% of the pre-coating value as the recognition cavities reopened pathways for probe diffusion to the underlying electrode **(Fig. 2d and Fig. S3)**. In contrast, the non-imprinted control (NIP, E) showed no comparable recovery, confirming that cavity formation, not generic film porosity, governs probe accessibility **(Fig. S2c)**.

Cavity formation was verified using three orthogonal characterization techniques. AFM resolved a 4.73 nm step at the MIP–AuNS boundary (localized heights of 9.16 and 13.89 nm, extracted from unlevelled data to avoid distortion; average electrode height: 68.57 nm), while the surface roughness (R_q) increased by 51.9% after template extraction across three independent regions **(Fig. 2e,f and Fig. S4–S5)**. These consistent topographical changes across multiple regions structurally validate the uniform generation of molecularly imprinted cavities over the entire sensor interface. TOF-SIMS depth profiling identified the Py-specific C_4HN^+ fragment as a discrete ~60 nm-thick overlayer on the gold surface that was absent from bare AuNS **(Fig. 2g,h and Fig. S6)**. FT-IR (C=O, C=C, and N–H) together with XPS (emergent N1s and attenuated Au4f signals) further confirmed the formation of a conformal nitrogen-containing polymer layer. The C=O and O1s components additionally verified the overoxidized state of PPy, whose carbonyl and carboxyl groups become negatively charged at physiological pH and provide the hydrogen-bonding and cation-selective sites responsible for DA recognition **(Fig. 2i–k)**.

The recognition mechanism was further validated by excluding a common artefact arising from DA self-polymerization **(Fig. S7a, b)**. Because DA can oxidatively self-polymerize into insulating polydopamine (PDA), control experiments performed for ten cycles in DA-only solutions containing up to 5.0 mM DA produced no measurable changes in either I_{pc} or I_{pa} **(Fig. S7c-g)**. In contrast, passive immersion in DA solution generated an insulating PDA layer that strongly inhibited electron transfer **(Fig. S7h-l)**. These results demonstrate that the electropolymerization conditions preferentially promote Py-derived imprinted-film growth while effectively suppressing PDA deposition.

In this integrated architechture, the PPy conformal overlayer serves an in situ-formed mechanical anchor for the underlying AuNS. Electrodeposited gold typically exhibits weak adhesion to oxide substrates and is prone to detachment under repeated high-potential cycling-a limitation conventionally addressed using sputtered Cr/Ti adhesion layers. Although intrinsic PPy-gold interactions are weak on smooth surfaces, the high-curvature AuNS morphology promotes conformal wrapping and mechanical interlocking of the electropolymerized film. The mechanical anchoring effect was next evaluated under repetitive electrochemical stress (20 CV cycles, −0.2 to 1.2 V in PBS). SEM revealed that AuNS coverage decreased dramatically from 76.3% to 23.8%, whereas the MIP electrode remained largely unchanged **(Fig. 2l,m)**. Critically, AFM showed that the vertical dimensions of the remaining nanostructures were preserved in both groups **(Fig. 2n,o)**, indicating that gold loss occurs predominantly through wholesale physical detachment rather than gradual electrochemical dissolution, consistent with the detachment-dominated failure mode previously reported for supported AuNSs subjected to repeated potential cycling [57]. ICP-OES further corroborated this conclusion, with the PBS supernatant containing 55.85 μg mL^{-1} of gold released from the AuNS electrode compared with only 5.15 μg mL^{-1} from the MIP electrode, representing more than a tenfold reduction **(Fig. 2p)**. Consistent with this structural degradation, the AuNS electrode lost 82% of its response to 10 μM DA, whereas the MIP electrode fully retained its sensing performance **(Fig. 2q,r)**, directly demonstrating the mechanical anchoring role of the conformal PPy layer.

For practical operation in biofluids, suppression of nonspecific protein adsorption is equally critical. In 10% FBS-containing medium, the AuNS electrode retained only 5.6% of its response to 10 μM DA in PBS, consistent with severe passivation by adsorbed serum proteins **(Fig. 2s)**. Because the NIP electrode exhibited only a weak response to 10 μM DA, its antifouling behaviour was evaluated using 100 μM DA; even at this higher concentration, the NIP showed a similarly pronounced signal loss **(Fig. 2t)**. Accordingly, the NIP retention ratio is interpreted qualitatively and is not directly compared with those of the AuNS and MIP electrodes. In contrast, the MIP retained 71.8% of its PBS response **(Fig. 2u)**. This improved retention arises from two complementary mechanisms beyond molecular recognition itself. The sub-nanometre imprinted cavities permit diffusion of small DA molecules while excluding nanometre-scale serum proteins, whereas the hydrophilic overoxidized PPy surface further suppresses nonspecific protein adsorption. Consequently, the retention ratio (I_{medium}/I_{PBS}) dropped to 0.056 for the AuNS and 0.185 for the NIP electrodes, but reached 0.718 for the MIP electrode **(Fig. 2v,w)**. These results unequivocally demonstrate the dual function of the conformal PPy layer: it not only provides the

mechanical robustness required to prevent nanostructure delamination, as confirmed above, but also acts as a highly selective molecular-recognition interface that preserves robust analytical performance even under severely fouling biological conditions. The selectivity of the imprinted interface against structurally related neurotransmitters is discussed in Section 2.3.

2.2 Optimization of MIP fabrication parameters for enhanced sensing performance

Electropolymerization parameters determine the thickness, uniformity, and electrochemical properties of the resulting imprinted polymer film. The potential window for Py electropolymerization was first optimized by comparing the electrochemical characteristics of films prepared under different scan ranges **(Fig. S8a, b)**. Characterization with 5 mM $[Fe(CN)_6]^{3-/4-}$ revealed high redox currents for Groups A-C but substantial current attenuation for Groups D-F, indicating effective interfacial shielding following polymer formation **(Fig. S8c-e)**. Film formation occured only when the applied potential window encompassed the Py oxidation potential (~0.8 V), confirming that oxidative polymerization of Py is responsible for film growth, consistent with the PPy deposits observed by SEM in Groups D-F **(Fig. S9)**.

The resulting electrodes were subsequently evaluated for DA detection **(Fig. S10a)**. A characteristic DA oxidation peak appeared at approximately 0.2 V, and a measurable DA response was observed exclusively for Group D, whose potential window included this oxidation process **(Fig. S10b, c)**. By contrast, Groups E and F, which excluded the DA oxidation potential, produced no detectable response. Increasing the number of electropolymerization cycles from 10 to 20 within Group D further reduced the DA current, consistent with excessive film thickening that restricts template diffusion during imprinting and subsequently limits analyte accessibility. These results identify both the electropolymerization potential window and cycle number as key determinants of MIP performance.

Beyond these operational parameters, simultaneous electropolymerization of the template and monomer introduces an inherent balance between recognition-site formation and polymer growth **(Fig. 3a)**. Excessive template loading leads to surface crowding that limits Py polymerization, leaving the underlying AuNS incompletely encapsulated. Moreover, template aggregation can generate irregular and enlarged cavities, thereby reducing size and shape complementarity and compromising exclusion of larger interferents and serum proteins. Conversely, excessive monomer concentrations reduce cavity density, shifting the response toward non-specific adsorption characteristic of NIP electrodes, while the denser polymer network imposes greater mass-transfer resistance that suppresses analytical sensitivity. Optimization therefore seeks a balance between recognition-site density, molecular accessibility, and complete conformal coverage required for anti-fouling performance.

With the Py concentration fixed at 2 mM, the DA template concentration was varied from 0.1 to 5.0 mM **(Fig. S11)**. The 1.0 mM template produced the highest DA current in PBS **(Fig. 3b, c)**, whereas the 0.5 and 1.0 mM groups exhibited comparable responses in serum-containing medium **(Fig. 3d, e)**. Notably, however, the signal retention ratio of the 0.5 mM group was 1.63-fold higher than that of the 1.0 mM group **(Fig. 3f)**. The discrepancy between the absolute signal in PBS and the signal retention in biological

medium suggests that increasing template loading likely enlarges the imprinted cavities, thereby enhancing the initial current while reducing the size-selective exclusion of fouling species. Accordingly, 0.5 mM DA was selected as the optimal template concentration, providing the best balance between sensitivity and anti-fouling performance.

Next, the Py concentration was varied between 1 and 10 mM **(Fig. 3g, h and Fig. S12).** A Py-free control, included as a no-polymer baseline, exhibited a severe cycle-dependent decrease in the absolute DA signal in PBS. This sharp decline confirms that, in the absence of Py, the unprotected AuNSs undergo progressive physical delamination during the repeated potential cycling required for MIP electrode fabrication. Moreover, the remaining AuNS lost virtually all DA response in serum-containing medium (signal retention ratio approximately 0.04-0.05) irrespective of the number of electropolymerization cycles, confirming that, in the absence of a conformal imprinted polymer layer, the gold surface becomes almost completely passivated by serum proteins (**Fig. S13a-e**; see Section 2.1). At 1 mM Py, the PBS response was maximal but decreased sharply in medium, indicating that the resulting film was insufficiently thick to provide complete coverage of the gold surface. Conversely, increasing the Py concentration to 10 mM reduced the DA response in both PBS and medium, consistent with increased mass-transfer resistance through an excessively thick polymer layer. The signal retention ratio reached its maximum between 2 and 5 mM Py, with 5 mM providing the greatest resistance to biofouling without markedly compromising sensitivity **(Fig. 3i-k)**. Within this concentration range, ten electropolymerization cycles consistently produced the highest DA response under both buffer and biological conditions and were therefore selected.

Template extraction conditions were finally optimized by varying the methanol (MeOH)-to-acetic acid volume ratio **(Fig. 3l, m)**. A MeOH:acetic acid ratio of 6:4 (v/v) maximized the signal retention ratio while preserving the structural and electrochemical integrity of the PPy layer **(Fig. 3n)**. In contrast, increasing the acetic acid fraction to 50% reduced the absolute DA current in both PBS and serum-containing medium and lowered the signal retention ratio by approximately 30%, consistent with hydrolytic degradation of the overoxidized PPy network under strongly acidic conditions. Accordingly, a 6:4 (v/v) extraction solution was selected for all subsequent experiments **(Fig. 3o)**. The DA response reached a steady-state plateau within approximately 3 min of incubation **(Fig. 3p, q)**. The optimized fabrication protocol, consisting of 0.5 mM DA, 5 mM Py, ten electropolymerization cycles, template extraction using MeOH/acetic acid (6:4, v/v), and a 3 min incubation period, was employed throughout the remainder of this study.

2.3 Analytical performance of the MIP sensor

The analytical performance of the optimized MIP sensor was first evaluated under cell-free conditions. In PBS, the DA oxidation current increased linearly over the concentration range of 0.01–20.0 μM (R^2 = 0.991; y = 2.14x + 0.36), yielding a limit of detection (LOD) of 57.4 nM calculated using the 3.3σ/slope criterion, where σ denotes the standard deviation of the blank response **(Fig. 4a, b)**. In medium supplemented with 10% FBS, the sensor exhibited a linear dynamic range of 0.05-20 μM (R^2 = 0.999),

with an LOD of 83.6 nM **(Fig. 4c, d)**. The modest increase in LOD under biological conditions is consistent with a small residual background arising from non-specific adsorption. Nevertheless, both values remain well below the sub-micromolar DA concentrations typically released by cultured neurons, demonstrating physiologically relevant analytical sensitivity. In contrast, the NIP electrode produced no discernible DA response even at elevated analyte concentrations **(Fig. S14a-c)**, confirming that molecular recognition and analyte accessibility originate from the imprinted cavities rather than the polymer matrix itself.

Analytical selectivity was evaluated against representative interferents associated with neurotransmission and DA biosynthesis, including norepinephrine (NE), serotonin (5-HT), epinephrine (EPI), L-3,4-dihydroxyphenylalanine (L-DOPA), and tyrosine (TYR) **(Fig. 4e)**. When each analogue was tested individually at 10 μM in PBS, only negligible responses were observed, except for slight cross-reactivity with NE, consistent with its close structural similarity to DA and its nearly identical oxidation potential **(Fig. 4f, g)**. Importantly, in a mixed solution containing all interferents, the DA signal remained essentially unchanged. Under the corresponding 10% FBS condition, the sensor retained approximately 70.1% of its original response, demonstrating selective DA detection even in protein-rich biological media. By comparison, the AuNS electrode responded indiscriminately to multiple neurotransmitters in PBS, resulting in severe peak overlap and poor electrochemical resolution **(Fig. S15a, b)**, while its responses in serum-containing medium were almost completely abolished by biofouling, precluding selective detection.

The molecular origin of this selectivity was further investigated by TOF-SIMS, which quantified the relative adsorption of each analyte on the imprinted interface **(Fig. S16a-c)**. Among the analytes examined, all of which share a C_6 aromatic framework, only DA exhibited increased adsorption (+17.5%), whereas 5-HT (-61.2%), EPI (-49.8%), NE (-53.8%), TYR (-92.5%), and L-DOPA (-48.4%) all showed substantially reduced adsorption **(Fig. S17a-c)**. These results demonstrate that molecular recognition is governed by the combined effects of cavity geometry and hydrogen-bonding interactions rather than structural similarity alone. Notably, although NE exhibited strongly reduced adsorption (-53.8%), it generated a small electrochemical response. These observations are not contradictory but instead reflect two distinct processes: adsorption measurements report preferential cavity binding, whereas the residual electrochemical signal arises from the near coincidence of the NE and DA oxidation potentials during faradaic detection. Together, these complementary measurements consistently support highly selective molecular recognition of DA.

Reliable biological monitoring further requires sustained analytical performance during repeated operation. A single MIP electrode subjected to ten successive template extraction and DA detection cycles exhibited highly reproducible responses with minimal signal variation **(Fig. 4h, i)**, demonstrating the structural reversibility and durability of the imprinted recognition sites. Resistance to cumulative biofouling and electrode passivation was subsequently evaluated by performing 10 consecutive measurements in PBS and in 10% FBS-supplemented medium without intermediate template extraction **(Fig. 4j-n)**. Under biological conditions, the MIP electrode demonstrated exceptional operational stability.

Although a slight stepwise signal decrease occurred due to the inevitable accumulation of DA oxidation byproducts and serum proteins, the MIP electrode successfully retained 77.71% of its initial response even at the 10th consecutive cycle **(Fig. 4n)**. This robust signal retention markedly outperforms the AuNS electrode, which suffered an immediate signal attenuation in both environments. In PBS, the AuNS electrode lost 40.66% of its initial signal already by the second cycle, with the signal decreasing by 73.00% at the 10th cycle, indicating severe passivation of the AuNS electrode surface during repetitive electrochemical measurements **(Fig. 4o, p)**. This vulnerability was further exacerbated in the 10% FBS medium, where the AuNS electrode exhibited an immediate 24.37% signal drop at the second cycle, culminating in 65.14% loss by the 10th cycle **(Fig. 4q, r)**. These results demonstrate that the combination of reversible molecular recognition and a biofouling-resistant interface preserves analytical performance during repeated measurements in complex biological media, supporting quantitative analysis of extracellular DA in cell culture supernatants.

2.4 Quantitative monitoring of extracellular DA during neuronal differentiation

SH-SY5Y cells are among the most widely used *in vitro* models of DAergic neurons. The sequential retinoic acid (RA)/brain-derived neurotrophic factor (BDNF) differentiation protocol employed here has been reported to promote robust neurite maturation together with pronounced upregulation of DAergic markers among commonly used differentiation strategies **(Fig. 5a)**. Although differentiated SH-SY5Y cells retain a degree of catecholaminergic heterogeneity and therefore do not fully recapitulate primary DAergic neurons, they provide a well-established and experimentally tractable model for evaluating extracellular DA release. During the 12-day differentiation period, the cells progressively developed an extensive neuritic network **(Fig. S18)**. Immunocytochemistry confirmed progressive acquisition of a mature DAergic phenotype **(Fig. 5b)**. The neuronal marker TUJ1 increased by 1.22-fold following RA treatment and by 6.58-fold after subsequent BDNF exposure, whereas the DAergic markers TH and DAT increased by up to 15.87-fold and 79.47-fold, respectively, relative to undifferentiated controls **(Fig. 5c-e)**. These phenotypic changes were further supported by coordinated transcriptional upregulation of MAP2, SYN1, SYP, EN1, TH, and DAT **(Fig. 5f-h)**.

Before applying the MIP sensor to the measurement of cell-derived DA, we evaluated its electrochemical stability across the pH range relevant to biological measurements. Because DA oxidation involves a two-electron/two-proton process, its formal potential shifts by approximately −59 mV per pH unit at 25 °C according to the Nernst equation. Across the examined pH range (6.2–8.2), the bare gold electrode exhibited unstable peak currents, whereas the MIP sensor maintained nearly constant peak currents accompanied only by the expected Nernstian shift in oxidation potential **(Fig. S19a-g)**. These observations suggest that the imprinted overoxidized PPy layer provides a locally buffered chemical microenvironment that reduces the influence of bulk pH fluctuations on molecular recognition. This buffering effect is particularly advantageous given the well-established pH dependence of DA stability, thereby improving the reliability of measurements performed directly in biological media.

Having established the pH robustness of the sensor, we next sought to measure DA released from cells during DAergic differentiation using the MIP sensor **(Fig. 5i–j and Fig. S20a-d)**. DPV analysis revealed a gradual increase in the DA signal obtained from the MIP sensor over the 12-day differentiation period **(Fig. 5i)**. Furthermore, the concentration of DA released from the cells at each differentiation stage was calculated based on regression analysis performed under culture conditions that stimulated DA release. The analysis showed that undifferentiated cells released 1.62 μM DA, with the amount of released DA increasing by 6.2-fold during the first 3 days of differentiation. Specifically, the DA concentrations measured on days 3, 6, 9, and 12 were 10.0, 14.0, 18.2, and 25.5 μM, respectively. This progressive increase in DA release was consistent with the functional changes associated with the development of DAergic neurons during DAergic differentiation. To determine whether the DA concentrations measured using the MIP sensor accurately reflected the actual amounts released from the cells, we cross-validated the MIP sensor measurements using HPLC and ELISA with the same samples **(Fig. 5k–l and Fig. S21–S23)**. HPLC analysis yielded DA concentrations of 1.00, 8.68, 14.5, 18.9, and 23.7 μM on differentiation days 0, 3, 6, 9, and 12, respectively **(Fig. 5k)**. Consistent with the MIP sensor results, the HPLC measurements demonstrated a progressive increase in DA release throughout the differentiation period. Nevertheless, notable differences were observed between the two analytical methods. In particular, the variability in the HPLC measurements was, on average, 7.5-fold greater than that observed in the MIP sensor measurements. Moreover, within each differentiation time point, the DA concentration obtained from the first HPLC measurement was consistently the highest, whereas repeated measurements of the same sample resulted in a marked decrease in the calculated DA concentration. The magnitude of this variation reached up to 16.4-fold within the same sample. Given the susceptibility of DA to oxidation and the relatively long analysis time required for HPLC, these findings suggest that DA may have undergone oxidation during the analytical procedure, thereby increasing measurement variability and potentially resulting in an underestimation of the actual amount of DA released. Meanwhile, ELISA also revealed a gradual increase in DA release during the differentiation period, consistent with the trend observed using the MIP sensor. Specifically, the DA concentrations measured on differentiation days 0, 3, 6, 9, and 12 were 0.64, 6.73, 11.2, 15.1, and 23.5 μM, respectively **(Fig. 5l)**. Interestingly, the DA concentrations determined using ELISA were 1.08- to 2.51-fold lower than those obtained using the MIP sensor. This discrepancy may have resulted from interference by components of the cell culture medium with the binding between DA and the antibody during ELISA. A localized preconcentration effect within the imprinted cavities may also contribute to the higher signals observed with the MIP sensor.

We subsequently performed a more detailed statistical assessment of the agreement between the MIP sensor measurements and those obtained using HPLC and ELISA **(Fig. 5m–q)**. First, the DA concentrations obtained from each analytical method were converted into z-scores for comparison. No statistically significant differences were observed among the methods at any differentiation time point, indicating that the overall data trends were statistically comparable across the analytical methods **(Fig. 5m)**. Furthermore, to evaluate agreement in both the overall trends and the magnitudes of change measured by the different methods, linear regression and Bland–Altman analyses were performed **(Fig.**

5n–q). Linear regression analysis between the HPLC and MIP sensor results demonstrated a strong linear relationship, with a slope of 0.94 **(Fig. 5n)**. In addition, Bland–Altman analysis showed that all differences between the paired HPLC and MIP sensor measurements fell within the 95% limits of agreement, indicating a relatively small systematic bias between the two methods **(Fig. 5o)**. Similarly, linear regression analysis of the ELISA results yielded a slope of 1.11, indicating that the data obtained using ELISA followed a trend consistent with that observed using the MIP sensor **(Fig. 5p)**. Furthermore, Bland–Altman analysis showed that all paired differences between the MIP and ELISA measurements fell within the ±1.96 SD limits of agreement, demonstrating good agreement between the two analytical methods without substantial method-dependent discrepancies **(Fig. 5q)**.

Collectively, these results demonstrate that the developed MIP sensor enables highly accurate detection of DA released from living DAergic neurons. Moreover, compared with conventional analytical methods for measuring exocytotic DA, such as HPLC and ELISA, the MIP sensor provides a substantially faster and simpler sensing procedure. This capability is particularly advantageous for accurately quantifying the trace amounts of DA released from cells while minimizing analytical errors arising from its susceptibility to oxidation.

3 Conclusions

This work presents a sensor platform that integrates electrodeposited AuNSs with a DA-imprinted PPy layer through a simple, fully electrochemical fabrication process. The resulting architecture enables nondestructive electrochemical monitoring of DA release, while the imprinted PPy layer functions simultaneously as a molecular recognition interface and a mechanical anchoring layer. Through conformal encapsulation of the underlying AuNSs, the PPy layer prevents delamination during both fabrication and operation, thereby addressing the persistent trade-off between the high electrochemical activity of nanostructured gold and the mechanical durability required for molecularly imprinted sensing interfaces.

Optimization of the fabrication parameters enabled the formation of molecularly imprinted recognition cavities while preserving efficient analyte transport through the polymer layer. The optimized sensor achieved limits of detection of 57.4 nM in PBS and 83.6 nM in medium supplemented with 10% FBS. Whereas bare AuNS electrodes retained only 5.6% of their initial response in serum-containing medium, the imprinted sensor retained 71.8% of its initial response and effectively discriminated against structurally related electroactive interferents. These results demonstrate the combined advantages of molecular recognition, mechanical robustness, and resistance to biofouling.

When applied to living neuronal cultures, the sensor successfully monitored stimulus-evoked extracellular DA release throughout DAergic differentiation, and the measured concentrations were independently validated using HPLC and ELISA. These findings establish the MIP electrode as a practical, label-free, and minimally invasive platform for the quantitative analysis of extracellular DA in cell-culture supernatants. More broadly, the fully electrochemical anchoring strategy provides a

generalizable approach for integrating mechanically robust molecularly imprinted interfaces with nanostructured electrochemical electrodes. This strategy may be extended to longitudinal secretome analysis, functional assessment of neuronal maturation, quality control of cell-based therapeutics, and screening of neuroactive compounds. Future integration with multielectrode arrays and advanced three-dimensional neural models, including brain organoids and assembloids, may further enable spatially resolved and long-term monitoring of neurochemical dynamics in physiologically relevant *in vitro* systems.

4 Experimental Section

4.1 Materials and cells

Indium tin oxide (ITO)-coated glass substrates were obtained from U.I.D. (South Korea). All chemical reagents, including gold (III) chloride trihydrate ($HAuCl_4 \cdot 3H_2O$), pyrrole, phosphate-buffered saline (PBS, pH 7.4), dopamine hydrochloride (DA), serotonin hydrochloride (5-HT), epinephrine hydrochloride (EPI), norepinephrine hydrochloride (NE), L-3,4-dihydroxyphenylalanine (L-DOPA), tyrosine (TYR), acetic acid, methyl alcohol (MeOH), potassium ferricyanide ($K_3[Fe(CN)_6]$), and potassium nitrate (KNO_3), were purchased from Sigma-Aldrich (USA). The chemicals and drugs required for neuronal differentiation were also supplied by Sigma-Aldrich (USA). The SH-SY5Y human neuroblastoma cell line was provided by the American Type Culture Collection (ATCC, USA). All reagents for cell cultivation, including basal media and essential supplements, were purchased from Gibco (USA). All aqueous solutions were prepared using deionized (DI) water (18.2 MΩ·cm) purified through a Milli-Q system.

4.2Fabrication of MIP sensor

The ITO glass substrates were sequentially cleaned via sonication in 1% Triton X-100, deionized (DI) water, and 70% ethanol. Subsequently, a AuNS electrode was electrochemically deposited onto the cleaned ITO surface from a 5 mM $HAuCl_4$ aqueous solution using amperometry at a constant potential of -1.3 V for 120 s. The resulting AuNS electrodes were rinsed three times with DI water to remove any residual gold precursor. To synthesize the DA-imprinted polymer, various ratios of Py and DA were dissolved in PBS. The MIP layer was then electropolymerized onto the AuNS surface through cyclic voltammetry (CV) within a potential window of -0.2 V to 1.2 V at 100 $mV \cdot s^{-1}$ scan rate. Following the coating process, the electrodes were thoroughly rinsed with DI water. The encapsulated DA templates were subsequently extracted by immersing the electrodes in various MeOH:acetic acid mixtures overnight to create the molecularly imprinted cavities. Finally, the MIP sensors were washed multiple times with DI water and stored at 4 ℃ until further use. As a control, a NIP electrode was prepared following the same procedure but in the absence of the DA template during the electropolymerization step. Additionally, a PDA model was fabricated to evaluate the impact of spontaneous DA polymerization; this was achieved by incubating the AuNS electrode in a 10 mM Tris-HCl buffer (pH 7.2) containing 2 mg/mL DA at room temperature overnight.

4.3Physicochemical surface characterization of fabricated MIP sensor

To analyze the physical architecture of the MIP sensors, parameters including morphology, height, and surface roughness were systematically monitored. The surface morphology was visualized using field-emission scanning electron microscopy (FE-SEM, SIGMA, Carl Zeiss), while the nanostructure height and roughness were characterized via atomic force microscopy (AFM, NX-10 Complete AFM, Park Systems). For comprehensive chemical characterization, the molecular binding structures, elemental compositions, and depth-dependent ionic distributions of the fabricated MIP sensors were investigated. Functional group signatures, such as C=O, N-H, and C=C, were elucidated through Fourier-transform infrared spectroscopy (FT-IR). The elemental profiles of In, N, C, and Au were verified using X-ray photoelectron spectroscopy (XPS, K-alpha+, Thermo Fisher Scientific). Furthermore, depth profiling to track Si^+, C_4HN^+, In^+, and Au^+ ions was conducted using Time-of-Flight Secondary Ion Mass Spectrometry (TOF-SIMS, TOF-SIMS-5, ION-TOF). Finally, to quantify the amount of gold delaminated from the electrode surface during the electrochemical stress tests, the PBS supernatants were analyzed using an inductively coupled plasma-optical emission spectrometer (ICP-OES, iCAP PRO XP DUO, Thermo Fisher Scientific).

4.4Analysis of DA sensing

Sensitivity and selectivity are the two primary metrics used to characterize the performance of MIP sensor. To evaluate sensitivity, the MIP sensors were incubated with varying concentrations of DA ranging from 0.01 to 20.0 μM in either PBS, and 0.05 to 20.0 μM in 10% FBS-supplemented medium for 3 minutes. DPV was performed with a scan rate of 50 $mV \cdot s^{-1}$, a step voltage of 1 mV, and a sensitivity of 1 $mA \cdot V^{-1}$. The LOD for DA was calculated from the linear calibration curves using the formula $3.3\sigma/m$, where σ is the standard deviation of the blank and m is the slope of the curve. To assess selectivity, structurally similar neurotransmitters and DA precursors, including norepinephrine (NE), serotonin (5-HT), epinephrine (EPI), L-DOPA, and tyrosine (TYR), were employed as target interferents. Each candidate was incubated at a concentration of 10 μM under identical conditions to DA and subsequently detected via DPV. Furthermore, TOF-SIMS analysis was utilized to quantify the molecular adsorption affinity on the AuNS and MIP surfaces. The electrodes were incubated with 10 μM of each molecule at 4 °C overnight and gently rinsed with DI water to remove loosely bound species. The C_6 aromatic ring fragmentation ion was tracked and normalized to the Total Ion Count (TIC). The relative adsorption change (%) was then calculated to evaluate the binding affinity of each molecule relative to the MIP surface. Furthermore, to evaluate the reproducibility and operational stability (replication) of the sensors, DA sensing at a concentration of 10 μM was conducted using three independent electrodes (n = 3) for each group. Reproducibility was assessed by subjecting the MIP sensors to 10 repeated cycles of the DA incubation and template extraction process, with each step monitored via DPV. For the stability (replication) tests, 10 consecutive measurements of 10 μM DA were performed without any intervening extraction or washing steps. This comparative analysis was conducted across four distinct experimental groups, MIP-PBS, MIP-medium, AuNS-PBS, and AuNS-medium to investigate the long-term signal maintenance and resilience of the MIP architecture against surface fouling in both buffer and medium.

4.5Electrochemical detection of DA released from SH-SY5Y

To evaluate DA release from neuronal cells on MIP sensor, a KCl stimulation protocol was employed. Cells were first incubated for 1 h in culture medium containing 100 µM L-DOPA, a DA precursor, to promote intracellular DA synthesis. After incubation, the cells were rinsed thoroughly at least five times with fresh medium to remove residual L-DOPA. Subsequently, KCl stimulation was applied for 15 min under the following condition: 90 mM KCl in culture medium for neuronal cells. DA release was then detected using differential pulse voltammetry (DPV). Electrochemical recordings were performed with a step potential of 1 mV, a scan rate of 50 $mV \cdot s^{-1}$, and a sensitivity of 1 $mA \cdot V^{-1}$.

4.6HPLC analysis of DAergic differentiation of SH-SY5Y

DA released during SH-SY5Y cell differentiation was quantified by high-performance liquid chromatography (HPLC) using an Agilent Technologies 1260 Infinity II LC system. Samples were collected from differentiated SH-SY5Y cells at days DIV 0, 3, 6, 9, and 12. Prior to HPLC analysis, the collected samples were prepared using Amicon® Ultra centrifugal filter units with a 3 kDa molecular weight cut-off (MWCO) by centrifugation at 14,000 × g for 20 min. Chromatographic separation was performed on an InfinityLab Poroshell 120 EC-C18 column (4.6 × 150 mm, 4 µm; Agilent). The mobile phases consisted of 0.1% trifluoroacetic acid (TFA) in water as solvent A and 0.1% TFA in acetonitrile (ACN) as solvent B. The gradient elution program was as follows: 99% solvent A was maintained for 4 min, followed by 95% solvent A until 10 min. The gradient was then returned to 99% solvent A by 10.1 min and maintained at 99% solvent A until 20 min. The flow rate was set at 1.0 mL/min, and the injection volume was 30 µL. The column temperature was maintained at 30 °C. DA was detected at a wavelength of 280 nm, with a retention time of approximately 4.6 min.

4.7Biological analysis of DAergic differentiation of SH-SY5Y

To induce DAergic differentiation of SH-SY5Y cells, the MIP sensor substrates were sterilized prior to cell seeding through a series of procedures. The substrates, along with the attached chambers, were first immersed in 70% ethanol to disinfect their surfaces. They were then rinsed with distilled water more than three times and exposed to ultraviolet light for at least 30 minutes. After sterilization, SH-SY5Y cells were seeded onto each substrate at a density of 52,000 cells/cm^2. The cells were cultured in DMEM supplemented with 10% FBS at 37 °C under a 5% CO_2 atmosphere. Once the cells reached approximately 80% confluence, DAergic differentiation was initiated by sequential treatment with 10 µM retinoic acid from DIV 0 to DIV 6, followed by 50 µM BDNF from DIV 6 to DIV 12.

To confirm DAergic differentiation, the expression of proteins and genes associated with this differentiation process was evaluated using both qualitative and quantitative methods, including immunocytochemistry and RT-qPCR. In the immunocytochemistry assay, cells were first fixed with 10% neutral buffered formalin (NBF) for 15 minutes at room temperature. After fixation, the cells were treated with 1% Triton X-100 for 5 minutes to allow permeabilization, followed by incubation with antibodies specific to neurogenesis-related protein markers. For RT-qPCR analysis, cells were lysed, total RNA was

extracted, and complementary DNA (cDNA) was synthesized to determine whether the cells had committed to a DAergic lineage. Gene amplification was carried out using SYBR Premix Ex Taq (Takara) with the StepOnePlus real-time PCR system. The obtained threshold cycle values were analyzed using the Livak $2^{-\Delta\Delta Ct}$ method. Finally, gene expression levels were normalized against GAPDH, which was used as an internal housekeeping reference gene.

Declarations

Acknowledgements: This work was supported by the National Research Foundation of Korea (NRF) grant funded by the Korea government, the Ministry of Science and ICT (MSIT) (Grant No. NRF-2022R1A4A2000776 and NRF-2022R1A2C4002217) and the Nano & Material Technology Development Program through the NRF funded by the MSIT (Grant No. RS-2024-00410437).

Authors contributions:

Joon-Ha Park, Yeon-Woo Cho: Methodology, Software, Data curation, Validation, Formal analysis, Writing-original draft

Min-Ji Kang: Software, Data curation, Validation, Formal analysis, Writing-original draft

Eun-Cheol Kwak: Data curation, Formal analysis

Tae-Hyung Kim: Conceptualization, Investigation, Supervision, Funding acquisition, Project administration, Resources, Writing-review & editing

Data availability: The data that support the findings of this study are available from the corresponding author upon reasonable request.

Conflict of interest: The authors declare that they have no conflict of interest.

References

1. Kriks S, Shim JW, Piao J, Ganat YM, Wakeman DR, Xie Z, Carrillo-Reid L, Auyeung G, Antonacci C, Buch A, Yang L, Beal MF, Surmeier DJ, Kordower JH, Tabar V, Studer L (2011) Dopamine neurons derived from human ES cells efficiently engraft in animal models of Parkinson's disease. Nature 480:547–551. https://doi.org/10.1038/nature10648
2. Kikuchi T, Morizane A, Doi D, Magotani H, Onoe H, Hayashi T, Mizuma H, Takara S, Takahashi R, Inoue H, Morita S, Yamamoto M, Okita K, Nakagawa M, Parmar M, Takahashi J (2017) Human iPS cell-derived dopaminergic neurons function in a primate Parkinson's disease model. Nature 548:592–596. https://doi.org/10.1038/nature23664
3. Monzel AS, Smits LM, Hemmer K, Hachi S, Moreno EL, van Wuellen T, Jarazo J, Walter J, Brüggemann I, Boussaad I, Berger E, Fleming RMT, Bolognin S, Schwamborn JC (2017) Derivation of

human midbrain-specific organoids from neuroepithelial stem cells. Stem Cell Rep 8:1144–1154. https://doi.org/10.1016/j.stemcr.2017.03.010

4. Cho AN, Jin Y, An Y, Kim J, Choi YS, Lee JS, Kim J, Choi WY, Koo DJ, Yu W, Chang GE, Kim DY, Jo SH, Kim J, Kim SY, Kim YG, Kim JY, Choi N, Cheong E, Kim YJ, Je HS, Kang HC, Cho SW (2021) Microfluidic device with brain extracellular matrix promotes structural and functional maturation of human brain organoids. Nat Commun 12:4730. https://doi.org/10.1038/s41467-021-24775-5
5. Jin Y, Lee JS, Kim J, Min S, Wi S, Yu JH, Chang GE, Cho AN, Choi Y, Ahn DH, Cho SR, Cheong E, Kim YG, Kim HP, Kim Y, Kim DS, Kim HW, Quan Z, Kang HC, Cho SW (2018) Three-dimensional brain-like microenvironments facilitate the direct reprogramming of fibroblasts into therapeutic neurons. Nat Biomed Eng 2:522–539. https://doi.org/10.1038/s41551-018-0260-8
6. Cho AN, Jin Y, Kim S, Kumar S, Shin H, Kang HC, Cho SW (2019) Aligned brain extracellular matrix promotes differentiation and myelination of human-induced pluripotent stem cell-derived oligodendrocytes. ACS Appl Mater Interfaces 11:15344–15353. https://doi.org/10.1021/acsami.9b03242
7. Jeong E, Choi S, Cho SW (2023) Recent advances in brain organoid technology for human brain research. ACS Appl Mater Interfaces 15:200–219. https://doi.org/10.1021/acsami.2c17467
8. Shin H, An Y, Lee JH, Kim JH, Prasad R, Kim KT, Kang HC, Sun W, Cho SW, Cho IJ (2025) One-step drug screening system utilizing electrophysiological activity in multiple brain organoids. Adv Sci (Weinh) 12:e04913. https://doi.org/10.1002/advs.202504913
9. Yang L, Chueng STD, Li Y, Patel M, Rathnam C, Dey G, Wang L, Cai L, Lee KB (2018) A biodegradable hybrid inorganic nanoscaffold for advanced stem cell therapy. Nat Commun 9:3147. https://doi.org/10.1038/s41467-018-05599-2
10. Rathnam C, Chueng STD, Yang L, Lee KB (2017) Advanced gene manipulation methods for stem cell theranostics. Theranostics 7:2775–2793. https://doi.org/10.7150/thno.19443
11. Yang L, Lee JH, Rathnam C, Hou Y, Choi JW, Lee KB (2019) Dual-enhanced Raman scattering-based characterization of stem cell differentiation using graphene-plasmonic hybrid nanoarray. Nano Lett 19:8138–8148. https://doi.org/10.1021/acs.nanolett.9b03402
12. Yang L, Patel KD, Rathnam C, Thangam R, Hou Y, Kang H, Lee KB (2022) Harnessing the therapeutic potential of extracellular vesicles for biomedical applications using multifunctional magnetic nanomaterials. Small 18:2104783. https://doi.org/10.1002/smll.202104783
13. Chen X, Yu C, Guo M, Zheng X, Ali S, Huang H, Zhang L, Wang S, Huang Y, Qie S, Wang J (2019) Down-regulation of m6A mRNA methylation is involved in dopaminergic neuronal death. ACS Chem Neurosci 10:2355–2363. https://doi.org/10.1021/acschemneuro.8b00657
14. Meyyappan M (2015) Nano biosensors for neurochemical monitoring. Nano Converg 2:18. https://doi.org/10.1186/s40580-015-0049-3
15. Cho YW, Park JH, Lee KH, Lee T, Luo Z, Kim TH (2020) Recent advances in nanomaterial-modified electrical platforms for the detection of dopamine in living cells. Nano Converg 7:40. https://doi.org/10.1186/s40580-020-00250-7

16. Hussein MA, El-Said WA, Abu-Zied BM, Choi JW (2020) Nanosheet composed of gold nanoparticle/graphene/epoxy resin based on ultrasonic fabrication for flexible dopamine biosensor using surface-enhanced Raman spectroscopy. Nano Converg 7:15. https://doi.org/10.1186/s40580-020-00225-8
17. Bui MPN, Li CA, Seong GH (2012) Electrochemical detection of dopamine with poly-glutamic acid patterned carbon nanotube electrodes. BioChip J 6:149–156. https://doi.org/10.1007/s13206-012-6207-3
18. Suhito IR, Angeline N, Kim TH (2019) Nanomaterial-modified hybrid platforms for precise electrochemical detection of dopamine. BioChip J 13:20–29. https://doi.org/10.1007/s13206-019-3106-x
19. Tran TB, Son SJ, Min J (2016) Nanomaterials in label-free impedimetric biosensor: Current process and future perspectives. BioChip J 10:318–330. https://doi.org/10.1007/s13206-016-0408-0
20. De Benedetto GE, Fico D, Pennetta A, Malitesta C, Nicolardi G, Lofrumento DD, De Nuccio F, La Pesa V (2014) A rapid and simple method for the determination of 3,4-dihydroxyphenylacetic acid, norepinephrine, dopamine, and serotonin in mouse brain homogenate by HPLC with fluorimetric detection. J Pharm Biomed Anal 98:266–270. https://doi.org/10.1016/j.jpba.2014.05.039
21. Jackowska K, Krysinski P (2013) New trends in the electrochemical sensing of dopamine. Anal Bioanal Chem 405:3753–3771. https://doi.org/10.1007/s00216-012-6578-2
22. Bucher ES, Wightman RM (2015) Electrochemical analysis of neurotransmitters. Annu Rev Anal Chem (Palo Alto Calif) 8:239–261. https://doi.org/10.1146/annurev-anchem-071114-040426
23. Labib M, Sargent EH, Kelley SO (2016) Electrochemical methods for the analysis of clinically relevant biomolecules. Chem Rev 116:9001–9090. https://doi.org/10.1021/acs.chemrev.6b00220
24. Stewart AJ, Hendry J, Dennany L (2015) Whole blood electrochemiluminescent detection of dopamine. Anal Chem 87:11847–11853. https://doi.org/10.1021/acs.analchem.5b03345
25. Sabaté del Río J, Henry OYF, Jolly P, Ingber DE (2019) An antifouling coating that enables affinity-based electrochemical biosensing in complex biological fluids. Nat Nanotechnol 14:1143–1149. https://doi.org/10.1038/s41565-019-0566-z
26. Pattan-Siddappa G, Elugoke SE, Erkmen C, Kim S-Y, Ebenso EE. Flexible carbon cloth electrode: pioneering the future of electrochemical sensing devices. Adv Compos Hybrid Mater. 2025;8:263. https://doi.org/10.1007/s42114-025-01338-6
27. Madhuvilakku R, Jeong OC, Hong Y. Bimetallic Pd@CeO_2-decorated 2D-g-C_3N_4/calcium alginate conductive hydrogel: a multifunctional hybrid material for wearable electrochemical sensing of serotonin. Adv Compos Hybrid Mater. 2025;8:395. https://doi.org/10.1007/s42114-025-01459-y
28. Dong W, Chen X. Research progress of wearable electrochemical biosensors based on metal–organic frameworks (MOFs) for sweat detection. Adv Compos Hybrid Mater. 2025;8:310. https://doi.org/10.1007/s42114-025-01357-3
29. Huang S, Li H, Yang M, Liu X, Fang Y, Xiao Q, Zhang Y. MX/MWCNTs composite material aids new strategy for HBV-DNA electrochemical biosensor: achieving multi-level signal amplification and

unlabeled detection. Adv Compos Hybrid Mater. 2025;8:127. https://doi.org/10.1007/s42114-025-01215-2

30. Karimi-Maleh H, Zhang Z, Zare N, Karaman O, Wen Y, Wu T, Zhong N, Fu L. A novel disposable dual-sensing platform based on DNA-aptamer amplified with gold nanoparticles/Nb_4C_3-MXene for simultaneous detection of lead and cadmium. Adv Compos Hybrid Mater. 2025;8:220. https://doi.org/10.1007/s42114-025-01216-1
31. Hwang MT, Park I, Heiranian M, Taqieddin A, You S, Faramarzi V, Pak AA, van der Zande AM, Aluru NR, Bashir R (2021) Ultrasensitive detection of dopamine, IL-6 and SARS-CoV-2 proteins on crumpled graphene FET biosensor. Adv Mater Technol 6:2100712. https://doi.org/10.1002/admt.202100712
32. Park I, Lim J, You S, Hwang MT, Kwon J, Koprowski K, Kim S, Heredia J, Stewart de Ramirez SA, Valera E, Bashir R (2021) Detection of SARS-CoV-2 virus amplification using a crumpled graphene field-effect transistor biosensor. ACS Sens 6:4461–4470. https://doi.org/10.1021/acssensors.1c01937
33. Jankelow A, Chen CL, Cowell TW, Espinosa de los Monteros J, Bian Z, Kindratenko V, Koprowski K, Darsi S, Han HS, Valera E, Bashir R (2024) Multiplexed electrical detection of whole viruses from plasma in a microfluidic platform. Analyst 149:1190–1201. https://doi.org/10.1039/D3AN01510F
34. Lim J, Koprowski K, Stavins R, Xuan N, Hoang TH, Baek J, Kindratenko V, Khaertdinova L, Kim AY, Do M, King WP, Valera E, Bashir R (2024) Point-of-care multiplex detection of respiratory viruses. ACS Sens 9:4058–4068. https://doi.org/10.1021/acssensors.4c00992
35. Valera E, Jankelow A, Lim J, Kindratenko V, Ganguli A, White K, Kumar J, Bashir R (2021) COVID-19 point-of-care diagnostics: Present and future. ACS Nano 15:7899–7906. https://doi.org/10.1021/acsnano.1c02981
36. Ostovan A, Arabi M, Wang Y, Li J, Li B, Wang X, Chen L (2022) Greenificated molecularly imprinted materials for advanced applications. Adv Mater 34:2203154. https://doi.org/10.1002/adma.202203154
37. Ma S, Wan Z, Wang C, Song Z, Ding Y, Zhang D, Chan CLJ, Shu L, Huang L, Yang Z, Wang F, Bai J, Fan Z, Lin Y (2024) Ultra-sensitive and stable multiplexed biosensors array in fully printed and integrated platforms for reliable perspiration analysis. Adv Mater 36:2311106. https://doi.org/10.1002/adma.202311106
38. Elbadawi M, Ong JJ, Pollard TD, Gaisford S, Basit AW (2021) Additive manufacturable materials for electrochemical biosensor electrodes. Adv Funct Mater 31:2006407. https://doi.org/10.1002/adfm.202006407
39. Li Y, Luo L, Kong Y, George S, Li Y, Guo X, Li X, Yeatman E, Davenport A, Li Y, Li B (2024) A point-of-care sensing platform for multiplexed detection of chronic kidney disease biomarkers using molecularly imprinted polymers. Adv Funct Mater 34:2316865. https://doi.org/10.1002/adfm.202316865

40. Chen Y, Hu X, Liang Q, Wang X, Zhang H, Jia K, Li Y, Zhang A, Chen P, Lin M, Qiu L, Peng H, He S (2024) Large-scale flexible fabric biosensor for long-term monitoring of sweat lactate. Adv Funct Mater 34:2401270. https://doi.org/10.1002/adfm.202401270
41. Kim KS, Lee HS, Yang JA, Jo MH, Hahn SK (2009) The fabrication, characterization and application of aptamer-functionalized Si-nanowire FET biosensors. Nanotechnology 20:235501. https://doi.org/10.1088/0957-4484/20/23/235501
42. An T, Kim KS, Hahn SK, Lim G (2010) Real-time, step-wise, electrical detection of protein molecules using dielectrophoretically aligned SWNT-film FET aptasensors. Lab Chip 10:2052–2056. https://doi.org/10.1039/C005276K
43. Lee HS, Kim KS, Kim CJ, Hahn SK, Jo MH (2009) Electrical detection of VEGFs for cancer diagnoses using anti-vascular endotherial growth factor aptamer-modified Si nanowire FETs. Biosens Bioelectron 24:1801–1805. https://doi.org/10.1016/j.bios.2008.08.036
44. Kong WH, Sung DK, Kim KS, Jung HS, Gho EJ, Yun SH, Hahn SK (2012) Self-assembled complex of probe peptide–E. coli RNA I conjugate and nano graphene oxide for apoptosis diagnosis. Biomaterials 33:7556–7564. https://doi.org/10.1016/j.biomaterials.2012.06.086
45. Kang MS, Cho E, Choi HE, Amri C, Lee JH, Kim KS (2023) Molecularly imprinted polymers (MIPs): Emerging biomaterials for cancer theragnostic applications. Biomater Res 27:45. https://doi.org/10.1186/s40824-023-00388-5
46. Haupt K, Mosbach K (2000) Molecularly imprinted polymers and their use in biomimetic sensors. Chem Rev 100:2495–2504. https://doi.org/10.1021/cr990099w
47. BelBruno JJ (2019) Molecularly imprinted polymers. Chem Rev 119:94–119. https://doi.org/10.1021/acs.chemrev.8b00171
48. Chen L, Wang X, Lu W, Wu X, Li J (2016) Molecular imprinting: Perspectives and applications. Chem Soc Rev 45:2137–2211. https://doi.org/10.1039/C6CS00061D
49. Mintz Hemed N, Leal-Ortiz S, Zhao ET, Melosh NA (2023) On-demand, reversible, ultrasensitive polymer membrane based on molecular imprinting polymer. ACS Nano 17:5632–5643. https://doi.org/10.1021/acsnano.2c11618
50. Chen S, Liu H, Liu S, Wang P, Zeng S, Sun L, Liu L (2018) Transparent and waterproof ionic liquid-based fibers for highly durable multifunctional sensors and strain-insensitive stretchable conductors. ACS Appl Mater Interfaces 10:4305–4314. https://doi.org/10.1021/acsami.7b17790
51. Dandegaonkar G, Ahmed A, Sun L, Adak B, Mukhopadhyay S (2022) Cellulose based flexible and wearable sensors for health monitoring. Mater Adv 3:3766–3783. https://doi.org/10.1039/D1MA01210J
52. Smith AT, LaChance AM, Zeng S, Liu B, Sun L (2019) Synthesis, properties, and applications of graphene oxide/reduced graphene oxide and their nanocomposites. Nano Mater Sci 1:31–47. https://doi.org/10.1016/j.nanoms.2019.02.004
53. Jia L, Zhou S, Ahmed A, Yang Z, Liu S, Wang H, Li F, Zhang M, Zhang Y, Sun L (2023) Tuning MXene electrical conductivity towards multifunctionality. Chem Eng J 475:146361.

https://doi.org/10.1016/j.cej.2023.146361

54. Hu M, Gao Y, Jiang Y, Zeng H, Zeng S, Zhu M, Xu G, Sun L (2021) High-performance strain sensors based on bilayer carbon black/PDMS hybrids. Adv Compos Hybrid Mater 4:514–520. https://doi.org/10.1007/s42114-021-00226-z
55. Todeschini M, Fanta ABS, Jensen F, Wagner JB, Han A (2017) Influence of Ti and Cr adhesion layers on ultrathin Au films. ACS Appl Mater Interfaces 9:37374–37385. https://doi.org/10.1021/acsami.7b10136
56. Tonelli D, Scavetta E, Gualandi I (2019) Electrochemical deposition of nanomaterials for electrochemical sensing. Sensors (Basel) 19:1186. https://doi.org/10.3390/s19051186
57. Chauhan P, Hiekel K, Diercks JS, Herranz J, Saveleva VA, Khavlyuk P, Eychmüller A, Schmidt TJ (2022)
Electrochemical surface area quantification, CO_2 reduction performance, and stability studies of unsupported three-dimensional Au aerogels versus carbon-supported Au nanoparticles. ACS Mater Au 2:278–292. https://doi.org/10.1021/acsmaterialsau.1c00067

Figures

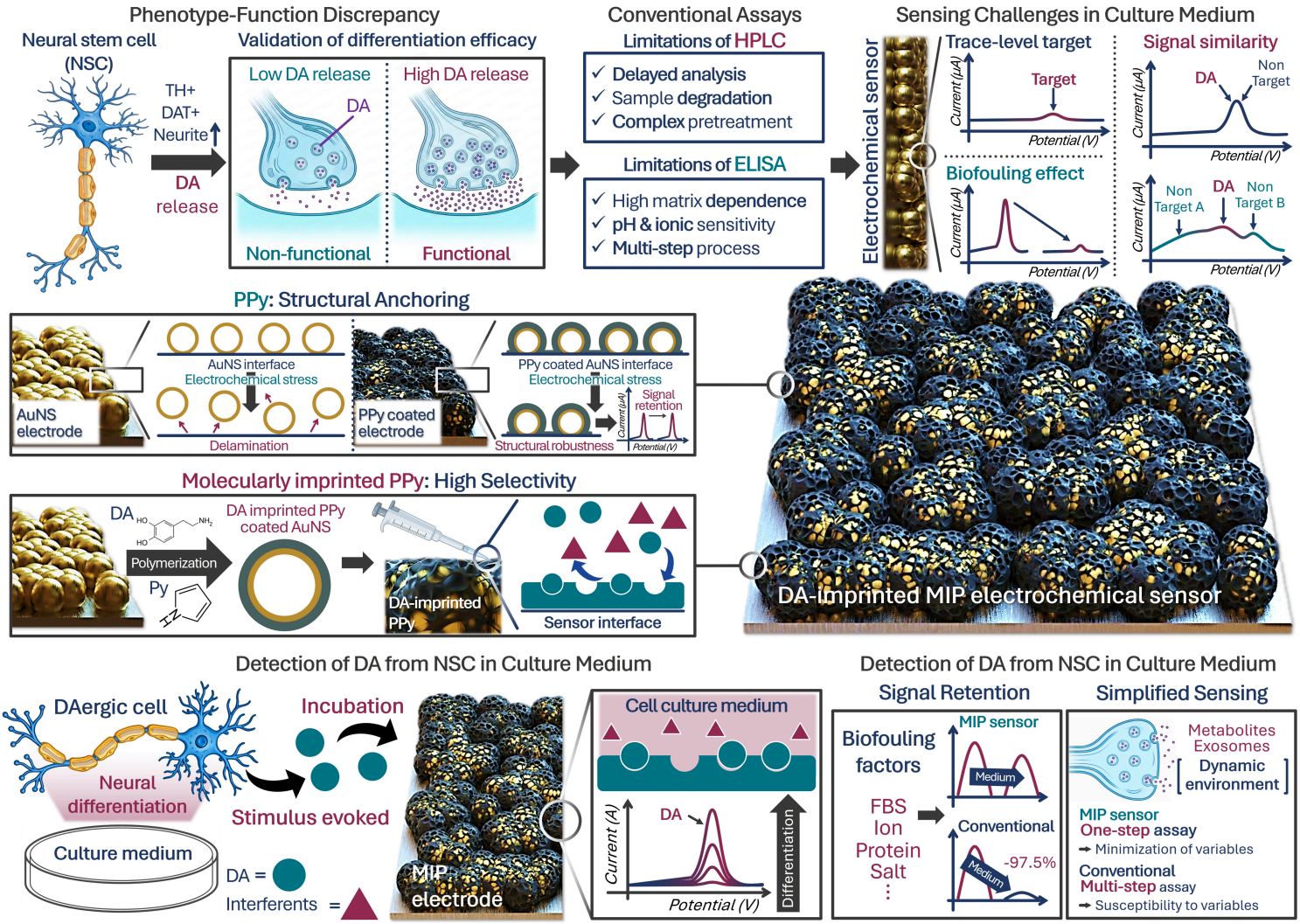


Figure 1

Schematic illustration of structurally anchored, DA-imprinted electrochemical sensor for quantifying cell-secreted DA.

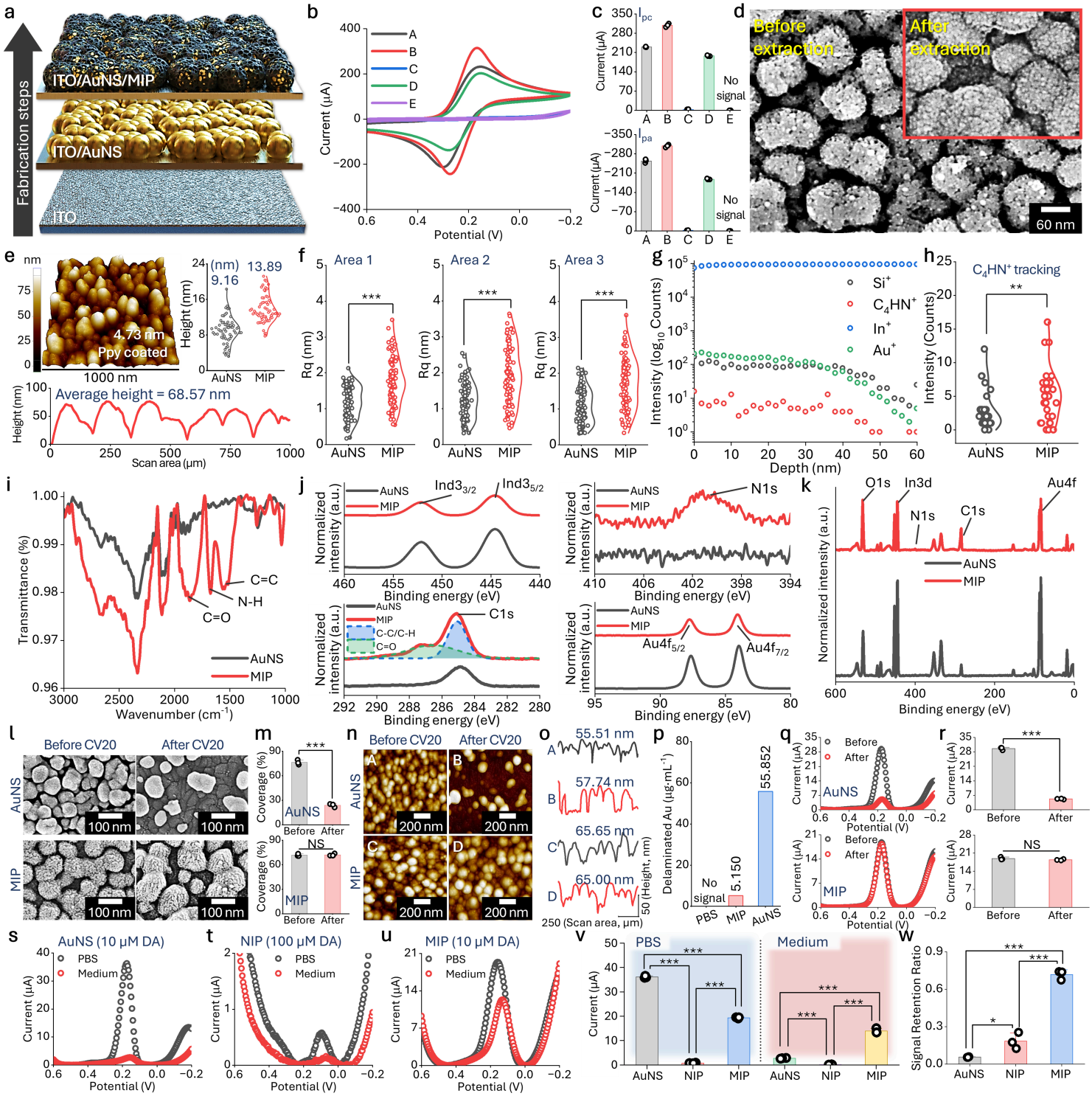


Figure 2

Structural, chemical, and electrochemical validation of MIP sensor. **a** Schematic of the sequential fabrication steps (A: ITO electrode, B: ITO/AuNS electrode, C: ITO/AuNS/MIP electrode before template

extraction, D: ITO/AuNS/MIP electrode after template extraction, E: NIP). **b** Electrochemical properties of each fabrication step. **c** Peak current analysis derived from b. **d** SEM images of the MIP surface before and after DA template extraction. **e** AFM 3D topography revealing an average height of 68.57 nm. The height difference between the underlying AuNS and the MIP layer confirms a precisely controlled PPy coating thickness of 4.73 nm. **f** Comparison of surface roughness (Rq) before and after extraction, confirming an increased surface area. **g** TOF-SIMS depth profiling of the MIP electrode surface. **h** Quantitative tracking of the Py-specific C_4HN^+ fragment. **i** FT-IR spectra identifying functional groups in the MIP layer. **j** High-resolution XPS spectra (Ind, C1s, N1s, and Au4f). **k** XPS survey spectra validating the chemical composition. **l** SEM images and **m** corresponding surface coverage quantification of the bare AuNS and MIP electrodes before and after the applied electrochemical stress. **n** AFM topographical images and **o** cross-sectional height profiles, showing the retention of localized vertical dimensions. **p** ICP-OES quantification of delaminated gold in the PBS supernatant after 20 CV cycles, validating the severe physical detachment of the bare AuNS. **q** Electrochemical responses to 10 µM DA and **r** corresponding peak current comparisons before and after the stress test. **s** DPV response of the AuNS electrode to 10 µM in PBS and 10% FBS-supplemented medium. **t** DPV response of the NIP electrode to 100 µM in PBS and 10% FBS-supplemented medium. **u** DPV response of the MIP electrode to 10 µM DA in PBS and 10% FBS-supplemented medium. **v** Peak current comparison illustrating the influence of biofouling. **w** Signal Retention Ratio (I_{Medium}/I_{PBS}) demonstrating anti-biofouling efficacy. All potentials are reported versus an Ag/AgCl reference electrode. Data are presented as mean ± SD (n = 3). Statistical significance was determined using an unpaired Student's t-test for (f, h m, r), and a one-way ANOVA followed by Tukey's test for (v, w) (NS: not significant, *: $p < 0.05$, **: $p < 0.01$, ***: $p < 0.001$).

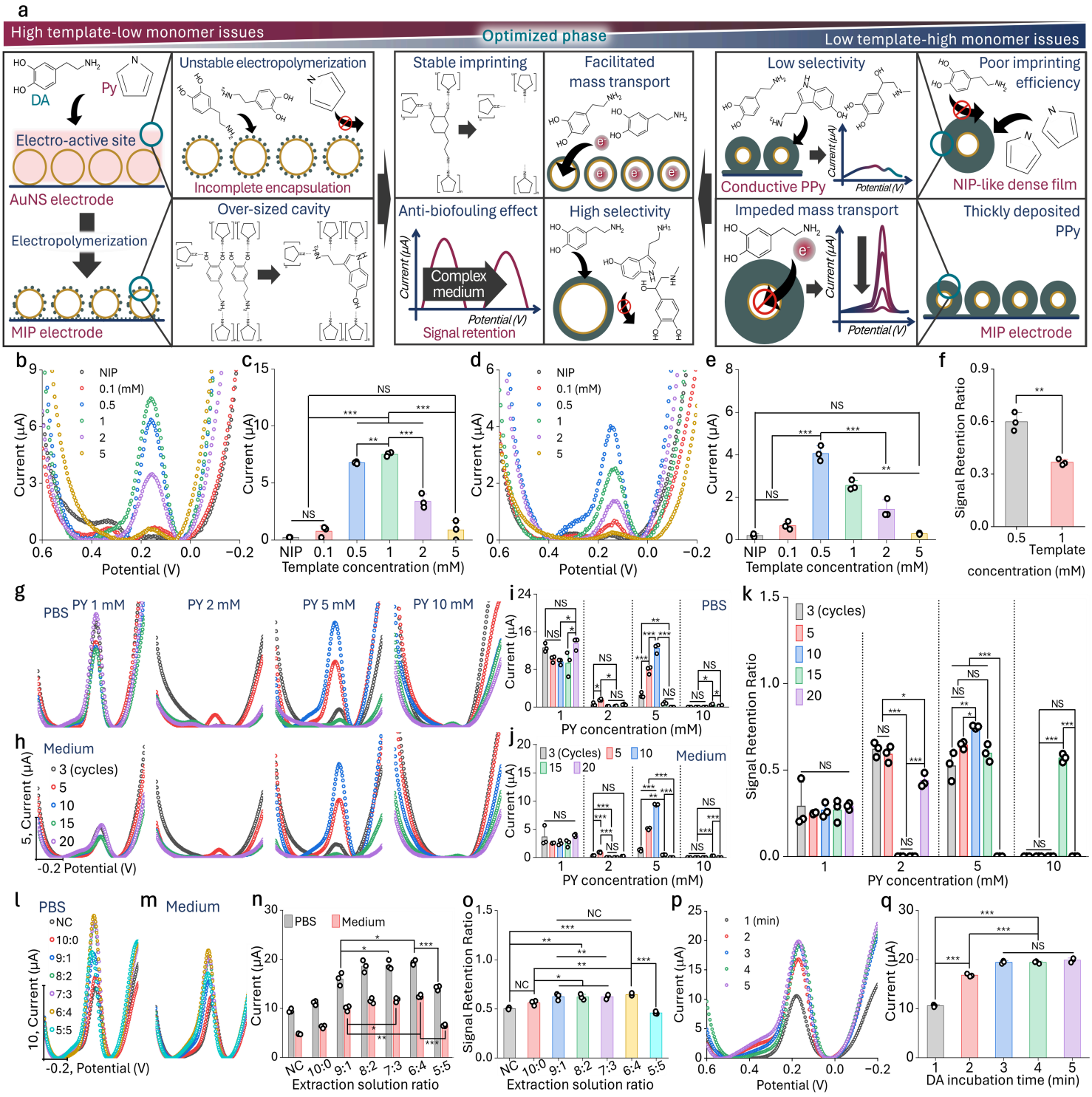


Figure 3

Systematic optimization of electropolymerization parameters. **a** Graphical illustration of the MIP fabrication optimization, addressing high template-low polymer issue and low template-high polymer issue to establish the optimized phase. **b** DPV profiles in PBS for various DA template concentration. **c**Quantitative evaluation of b. **d** DPV profiles in medium for various DA template concentration. **e** Quantitative evaluation of d. **f** Signal Retention Ratio comparison between the 0.5 and 1.0 mM template concentration groups. **g** DPV profiles in PBS across different Py concentrations and cycles numbers. **h**

DPV profiles in 10% FBS-supplemented medium across different Py concentrations and cycle numbers. **i** Quantitative evaluation of g. **j** Quantitative evaluation of h. **k** Signal Retention Ratio analysis as a function of Py concentration and cycle number. **l** DPV profiles in PBS for various template extraction solution ratios. **m** DPV profiles in 10% FBS-supplemented medium for various template extraction ratios. **n** Comparison of peak currents in PBS and medium across different extraction solution ratios (MeOH:acetic acid). **o** Signal Retention Ratio for various extraction solution compositions. **p** DPV profiles evaluating the effect of DA incubation time on the MIP surface. **q** Quantitative evaluation of p. All potentials are reported versus an Ag/AgCl reference electrode. Data are presented as mean ± SD (n = 3). Statistical significance was determined using a one-way ANOVA followed by Tukey's test for (c, e, i, j, k, n, o, q), and an unpaired Student's t-test for (f) (NS: not significant, *: $p < 0.05$, **: $p < 0.01$, ***: $p < 0.001$).

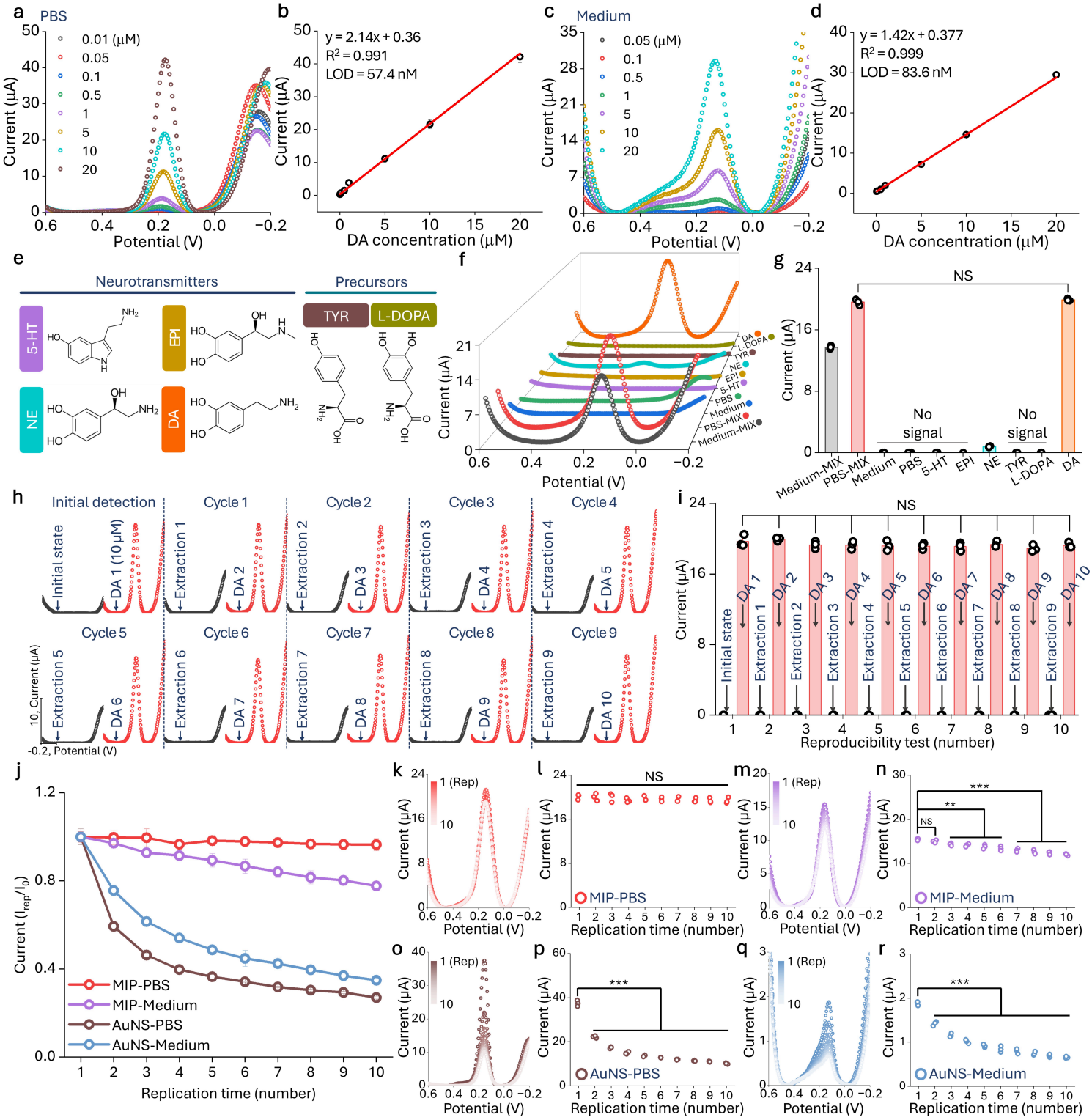


Figure 4

Detection of DA in cell-free configuration. **a** DPV plot for various DA concentration in PBS. **b** Linear calibration plot for DA in PBS. **c** DPV plot for various DA concentration in 10% FBS-supplemented medium. **d** Linear calibration plot for DA in 10% FBS-supplemented medium. **e** Chemical structures of neurotransmitters (5-HT, EPI, NE, DA) and precursors (TYR, L-DOPA) used in the selectivity assay. **f** DPV

plot indicating selective test of fabricated MIP sensor. **g** Quantitative evaluation of f. **h** DPV plot indicating 10 repeated cycles of template extraction and detection. **i** Quantitative evaluation of h. **j** Comparison of normalized current (I_{rep}/I_0) between MIP and AuNS electrode groups over 10 consecutive measurements. **k** DPV plot for the MIP-PBS group over 10 replication cycles. **l** Quantitative evaluation of k. **m** DPV plot for the MIP-medium group over 10 replication cycles. **n** Quantitative evaluation of m. **o** DPV plot for the AuNS-PBS group over 10 replication cycles. **p** Quantitative evaluation of o. **q** DPV plot for the AuNS-medium group over 10 replication cycles. **r** Quantitative evaluation of q. All potentials are reported versus an Ag/AgCl reference electrode. Data are presented as mean ± SD (n = 3). Statistical significance was determined using a one-way ANOVA followed by Tukey's test (NS: not significant, *: $p < 0.05$, **: $p < 0.01$, ***: $p < 0.001$).

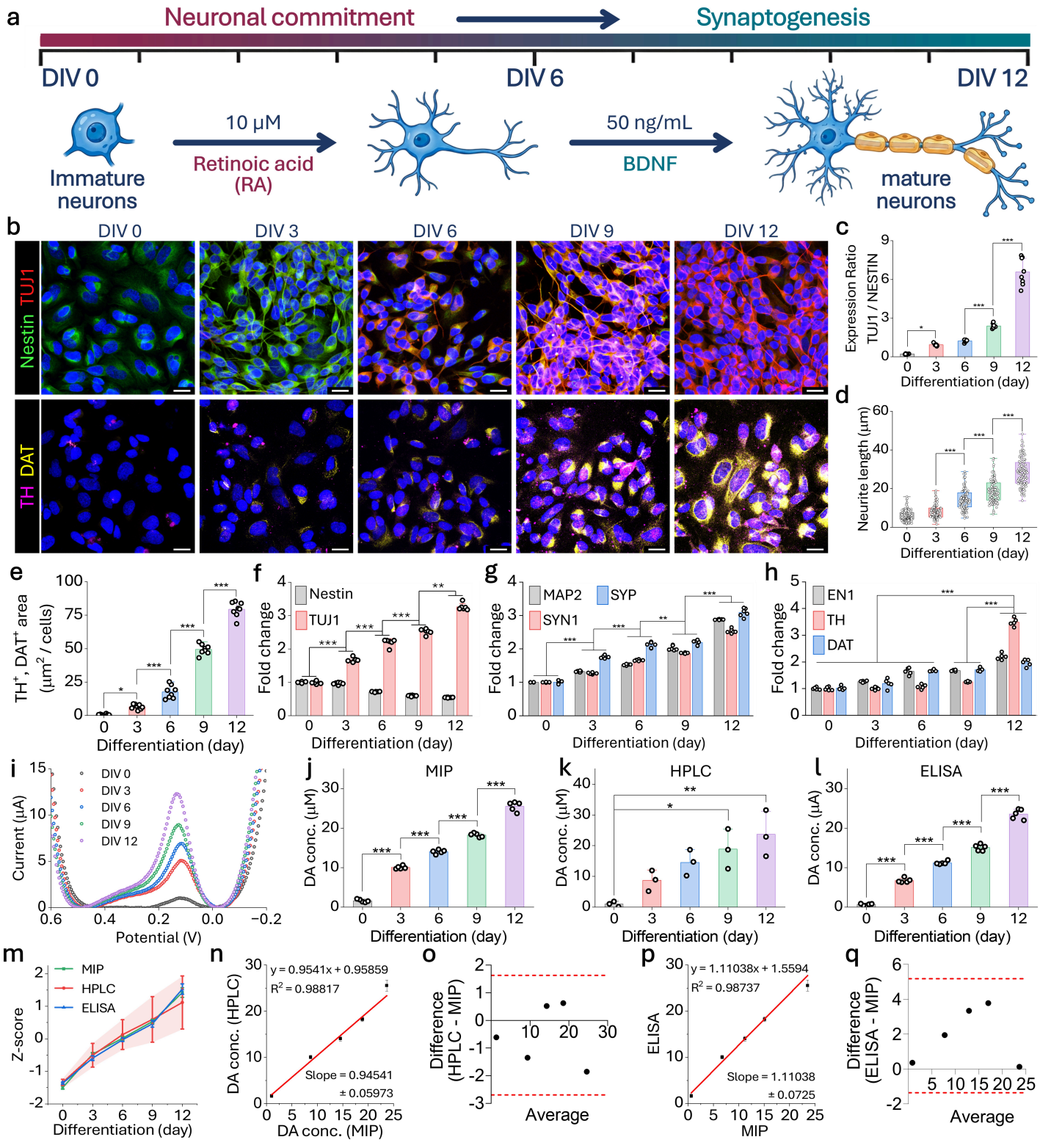


Figure 5

Real-time monitoring of exocytotic DA release during DAergic differentiation using the MIP sensor. **a** Schematic illustration of DAergic differentiation induced by the combined treatment of retinoic acid (RA) and brain-derived neurotrophic factor (BDNF). **b**Representative immunocytochemistry images of cells stained for Nestin, βIII-tubulin (TUJ1), tyrosine hydroxylase (TH), and DA transporter (DAT) during DAergic differentiation. **c** Quantitative analysis of the immunocytochemistry images stained for TUJ1

and Nestin. **d** Neurite lengths measured in Nestin- or TUJ1-positive cells. **e** Quantitative analysis of the immunocytochemistry images stained for TH and DAT. **f–h**PCR analysis of genes associated with DAergic differentiation, including genes related to early differentiation, neuronal maturation, and functional acquisition, respectively. **i** Differential pulse voltammetry (DPV) curves obtained using the MIP sensor in cell culture media collected following stimulation of DA release at different stages of DAergic differentiation. **j**DA signals derived from the DPV curves of the MIP sensor at each differentiation time point. **k-l** HPLC and ELISA analyses performed for cross-validation of DA measurements obtained using the MIP sensor. DA concentrations were independently quantified by HPLC and ELISA using aliquots of the same cell culture media collected at each differentiation time point. **m**Comparison of z-scores for DA release quantified by each analytical method across differentiation days. **n, o** Linear regression and Bland–Altman analyses of DA release quantified by HPLC and MIP. **p, q** Linear regression and Bland–Altman analyses of DA release quantified by ELISA and MIP. In the Bland-Altman analyses, the solid line represents the mean difference (bias), and the dashed lines indicate the upper and lower 95% limits of agreement (mean difference ± 1.96 SD). All potentials are reported versus an Ag/AgCl reference electrode. All scale bars represent 20 μm. Data are presented as mean ± SD (n = 3). Statistical significance was determined using a one-way ANOVA followed by Tukey's test (NS: not significant, *: $p < 0.05$, **: $p < 0.01$, ***: $p < 0.001$).

Supplementary Files

This is a list of supplementary files associated with this preprint. Click to download.

- ACHMSupportingInformationJ.H.ParkandY.W.Cho..docx
- S1.jpeg
- S2.jpeg
- S3.jpeg
- S4.jpeg
- S5.jpeg
- S6.jpeg
- S7.jpeg
- S8.jpeg
- S9.jpeg
- S10.jpeg
- S11.jpeg
- S12.jpeg
- S13.jpeg
- S14.jpeg
- S15.jpeg

- S16.jpeg
- S17.jpeg
- S18.jpeg
- S19.jpeg
- S20.jpeg
- GA.png
- S21.jpeg
- S22.jpeg
- S23.jpeg